Detection of virus particles by scattering field using multi-perspectives polarization modulation imaging method

Baoheng Guo,[1,5] **Bin Ni,**[1,5] **Xiao Jin,**[1] **Heng Zhang,**[1] **Hanwen Zhao,**[1] **Lianping Hou,**[2] **John H. Marsh,**[2] **Lei Dong,**[3] **Shanhu Li,**[4] **Jichuan Xiong,**[1,*] **and Xuefeng Liu**[1,*]

[1]*School of Electronic and Optical Engineering, Nanjing University of Science and Technology, Nanjing, Jiangsu, 210094, China*
[2]*James Watt School of Engineering, University of Glasgow, Glasgow, G12 8QQ, UK*
[3]*School of Life Science, Beijing Institute of Technology, Beijing, 100081, China*
[4]*Department of Cell Engineering, Beijing Institute of Biotechnology, Beijing, 100850, China*
[5]*B. Guo and B. Ni contributed equally to the manuscript*
*Corresponding author: liuxf1956@sina.com

Polarization parametric indirect microscopic imaging (PIMI) method, which employs a polarization modulated incidence illumination and fitting the far-field variation of polarization states of the scattered photons, is capable of direct identification of the sub-diffraction-scale structures and substances, such as the virus particles. However, in the present strategy, the optical elements which collect the scattered photons are nearly fixed above the sample, making the collected information relatively limited as the side-scattering photons are not fully utilized. To address this problem, we propose a multi-perspectives PIMI imaging method to maximize the collection of scattering photons from different spatial directions, which can obtain more information of optical anisotropy among particles. As a proof-of-concept study, virus detection using such method is performed theoretically and experimentally. Results reveal that the virus particles can be detected and determined more distinctly thanks to the set of PIMI images from different spatial angles, showing notable superiority to the previous scheme where only a plane PIMI image is derived from a fixed spatial direction. With the capability of acquiring more characteristics of the samples, the proposed multi-perspectives PIMI method can be applied in many fields such as morphological characterization and bio-sensing. © 2021 Optical Society of America

1. INTRODUCTION

The virus is a special kind of pathogen in which its associated diseases are one of the main threats to human health. For instance, the coronavirus disease 2019 (COVID-19) has given rise to millions of deaths worldwide so far, imposing significant influence on the human society [1,2]. The constant occurrence of new infection agents and strong ability of frequent virus mutation such as COVID-19 makes it difficult to control the virus-induced pandemics quickly and completely despite the policy of isolation and contact restriction [3].

Rapid and precise detection of different viruses is a critical technique for the control and prevention of pandemics. Fortunately, many virus detection methods have been developed and played positive roles, including the widely used method of nucleic acid detection and amplification technique such as polymerase chain reaction (PCR) [4], quantitative polymerase chain reaction (qPCR) [5], and real-time polymerase chain reaction (RT-PCR) [6], the immunoassays technique such as fluorescent antibody (FA) staining, hemagglutination inhibition, and immuno-peroxidase staining [7], DNA sequencing technique such as DNA microarrays [8], the mass spectrometric methods such as matrix-assisted laser desorption ionization time-of-flight (MALDI-TOF) [9]. In addition, microelectronics and microfluidics-based technologies include lab-on-a-chip (LOC), point of care (POC) testing [10], and surface plasmon resonance (SPR) sensing [11].

However, the previously mentioned indirect methods for virus detection still have drawbacks in regards to time consumption, relatively complex processing procedure, high cost, need of skilled operators and specific handling room. Compared with the contemporary methods for virus detecting, optical imaging holds great potential for fast and direct virus screening with the

advantages of intuitive detection, large field of view, low cost, and fast speed [12]. Due to its strong ability to resolve anisotropic features beyond the diffraction limit by detecting the variation of scattering photon states from the sample, polarization parametric indirect microscopic imaging (PIMI) has been applied in a variety of fields, including the attempt to identify virus particles [13]. The gold nanoparticles (AuNPs) aggregated with a virus particle can enhance the scattering signal [14-16] in PIMI imaging for the detection of virus particle, indicating the possibility of fast virus sensing in a wide-field view via the PIMI method. However, the present objective lens in the PIMI mechanical system which collects the photons scattered from the sample is located directly above the sample with a limited size, which means that a fraction of the side scattering signal is not collected. Moreover, only an individual plane PIMI image can be obtained after performing the measurement. Hence, shortcomings faced by the present PIMI strategy mainly include that the morphological nano-features of the analyte especially at the side edge are not fully included in the PIMI image, and the confidence level of determining the detected sample such as virus particles need to be improved because of the information limited by the plane image.

In this paper, we propose a new method to simulate the polarization modulated scattering field using a spherical monitor in Discontinuous Galerkin Time Domain (DGTD) with the PIMI method. The spherical monitor is used for detecting the scattering of polarization modulated field, which overcomes the previous shortcomings of less spatial dimension in scattering signal by plane detection, and can reveal more information about the interaction between nanoparticles and incident polarized light field in the side space. At the same time, the Stokes vector obtained in full space contains the complete scattering information of the nanoparticles which also provides a solid foundation for the subsequent Poincaré mapping to detect virus particles statistically. To verify the accuracy of the simulation, we calculate the polarized wavefront fields on the first surface of the objective lens from CCD images to compare with the simulated results on upper hemisphere.

To realize the full perspective observation of nanoparticles in the polarized scattering field by experiment, we plan to rotate the entire microscopic objective apparatus and cover the 2π steradian on the sphere and put them together for increased collection of useful information.

Hopefully, using the multi-perspectives PIMI method to collect the photons scattering information from the multi-angle spatial dimensions can provide more assistance for the effective detection of nanoparticles such as virus in the future.

2. METHODS OF MEASUREMENT

A. DGTD Theory

Numerical simulation methods are used to calculate the optical properties in nanoscale particles. Widely used methods include the Finite Difference Time Domain (FDTD) method and the Finite Element Method (FEM) currently. The FDTD is a fast and simple time-domain method for solving Maxwell's equations, but its accuracy is relatively low, only in second-order accuracy. In addition, this method needs to be limited to an inflexible orthogonal space with discrete grid, Yee-grid [17,18].

When solving problems concerning small geometric features or bending shapes, the finite element method allows flexible and discrete meshing of the physical system, and the spatial order of accuracy can be improved by using higher-order basis functions [19]. Hesthaven and Warburton applied the DGTD method to the electrodynamics [20,21]. In principle, the DGTD is a variant of traditional FEM. The main difference is that the basic function of the DGTD method is defined on only one element without any overlap with the adjacent elements, which effectively decouples the elements [22]. After performing all the time-consuming operations on each cell separately, the coupling between cells is reintroduced through the so-called numerical flux [23]. With this technique, the mathematical complexity of computation is reduced, allowing DGTD to efficiently handle the time-dependent problems. Therefore, the method of DGTD can simulate the spherical monitor and overcome the disadvantage of traditional FDTD which is not flexible and limited in the discrete mesh of orthogonal space. D. Shree simulated the scattering-field propagation of gold nanoparticles in the human epidermis and blood at different wavelengths based on the Mie scattering by the DGTD method [24].

The DGTD simulation takes place in the time domain and uses the Mie solution of Maxwell's equations to describe the scattering of plane waves by a homogeneous sphere:

$$\frac{\partial \overline{D}}{\partial t} = \nabla \times \overline{H}. \qquad (1)$$

$$\frac{\partial \overline{H}}{\partial t} = -\frac{1}{\mu_0} \nabla \times \overline{E}. \qquad (2)$$

$$\overline{D}(\vec{r}, \omega) = \varepsilon_0 \varepsilon_r(\vec{r}, \omega) \overline{E}(\vec{r}, \omega). \qquad (3)$$

$\overline{D}$ is the electric displacement vector. $\overline{H}$ is the magnetic field component. $\overline{E}$ is the electric field component. $\vec{r}$ is the space position vector. t is the time variable. ω is the time-frequency. ε_0 is the permittivity of vacuum. ε_r is the relative dielectric constant.

Another characteristic of DGTD is that it relies on strengthening the continuity of numerical flux on the plane f, not the components of the field as shown in Fig. 1 [25].
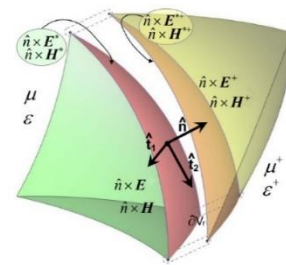

Fig. 1. Notation used to define numerical flux in a DGTD calculation.

Here, $\hat{n}$ is a unit vector that goes out of the element. E^* and H^* represent the electric and magnetic fields at the interface, and superscript "+" represents the adjacent field on a face element f. μ is the magnetic permeability. ε is the dielectric constant, and ∂V_f is the differential numerical flux.

In the following parts, we make use of the advantages of DGTD to implement a spherical monitor to collect the scattering information of polarization modulation, and show the strengths of the unstructured grids and computational efficiency.

B. PIMI Method

As shown in Fig. 2, the PIMI system mainly consists of polarizer, analyzer and microscopic objective. The polarizer adopts a linear polarizer that can rotate relative to the X-axis at an equal angle. The analyzer adopts a quarter wave plate whose fast axis is along the +X-axis, and the linear polarizer is at +45° relative to the +X-axis. Since we realized the detection of spherical light source in the simulation, we proposed to make the device able to rotate with respect to the X-axis and Y-axis in order to realize the whole perspective detection.
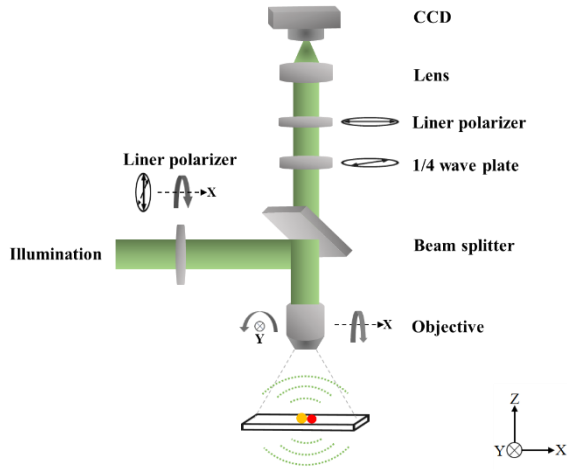

Fig. 2. The concept diagram of the PIMI system with full view acquisition.

The scattering field passing through the analyzer changes periodically by continuously rotating the polarizer relative to X-axis. The information of extinction angle φ and phase difference δ are included in the outgoing light intensity. The light intensity passing through the polarization system is expressed as [26]:

$$I = \frac{I_0}{2}\left[1 + \sin\left(2\omega t - 2\varphi\right)\sin\delta\right]. \tag{4}$$

I_0 is the intensity of incident light. ω and t are the angular frequency and time respectively. We can extract |sinδ| from this intensity expression by Fourier analysis of the expression above. $\delta = \delta_y - \delta_x$ is the phase difference between orthogonal components of the electric field. In Fig. 3(a), E_x and E_y are the amplitudes of x and y components respectively. a is the semi-major axis of ellipse. b is the semi-minor axis of ellipse. φ is the extinction angle and β is the elliptical angle. When rotating the polarizer through the total $\alpha_{\max} = 180°$ in N steps, the angle of step k is $\alpha_k = (k-1)\times(\alpha_{\max} / N)$, where k is chosen as 1, 2, 3,···, N. The intensity on detector is described by Eq. (4) and its derivation is written in the following form:

$$I_k = a_0 + a_1 \sin(2\alpha_k) + a_2 \cos(2\alpha_k). \tag{5}$$

$$a_0 = \frac{I_0}{2}, \ a_1 = \frac{1}{2}I_0 \sin\delta\cos 2\varphi, \ a_2 = -\frac{1}{2}I_0 \sin\delta\sin 2\varphi. \tag{6}$$

Here, parameters a_i (i =0, 1, 2) can be rewritten as:

$$a_0 = \sum_{k=1}^{N}\frac{1}{N}I_k, \ a_1 = \sum_{k=1}^{N}\frac{2}{N}I_k \sin\alpha_k, \ a_2 = \sum_{k=1}^{N}\frac{2}{N}I_k \cos\alpha_k. \tag{7}$$

The polarized parameters of different characteristics in samples can be obtained by Eqs. (5)-(7), such as the depolarization intensity parameter $I_{\mathrm{dp}} = a_0$, the extinction angle parameter $\varphi = \frac{1}{2}\arccos\left(a_1 / \sqrt{a_1^2 + a_2^2}\right)$ and the phase difference parameter $|\sin\delta| = \sqrt{a_1^2 + a_2^2} / a_0$.

Using the polarized parameters above and Jones matrix we can derive the following Stokes vector matrix representation of samples:

$$\begin{bmatrix} S_0 \\ S_1 \\ S_2 \\ S_3 \end{bmatrix} = \begin{bmatrix} I_{dp}\left(1+\sin\delta\right) \\ I_{dp}\left(1+\sin\delta\right)\cos 2\varphi \\ \sqrt{2}I_{dp}\left(1+\sin\delta\right)\sqrt{\sin 2\varphi}\cos\delta \\ \sqrt{2}I_{dp}\left(1+\sin\delta\right)\sqrt{\sin 2\varphi}\sin\delta \end{bmatrix}. \tag{8}$$

As shown in Fig. 3(b), the Poincaré sphere is usually used to represent all the possible polarized states of polarization modulated scattering field and it is a solid sphere with a radius of 1 unit. The points on the spherical surface represent fully polarized states which have the intensity of 1 unit, and the points inside the sphere represent partial polarization states, and the origin point of sphere represents unpolarized states. The Stokes vector of light can be written as [27]:

$$\mathbf{S} = \begin{bmatrix} S_0 \\ S_1 \\ S_2 \\ S_3 \end{bmatrix} = \begin{bmatrix} I \\ IP\mathbf{u} \end{bmatrix}. \tag{9}$$

$$P = \frac{\left(S_1^2 + S_2^2 + S_3^2\right)}{S_0}, \mathbf{u} = \begin{bmatrix} S_0 \\ S_1 \\ S_2 \end{bmatrix} = \frac{1}{IP}\begin{bmatrix} \cos\theta\cos\chi \\ \cos\theta\sin\chi \\ \sin\chi \end{bmatrix}. \tag{10}$$

I is the light intensity and $I = S_0$. P is the degree of polarization. $\mathbf{u}$ is the unit vector that defines the azimuth angle $\theta\left(0 \le \theta \le 2\pi\right)$ and polar angle $\chi\left(0 \le \chi \le 2\pi\right)$ in the Poincaré sphere.
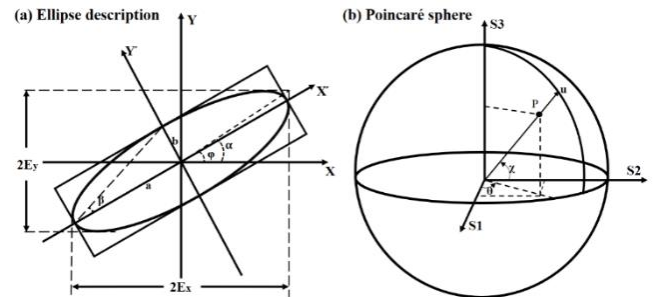

Fig. 3. Schematic description of the polarization parameters. (a) Definition of the extinction angle φ. (b) Polarized states represented in the Poincaré sphere.

In the PIMI method, the polarized scattering field is generated by the coupling between incident light field from different angles and the changes among structural properties in samples.

This method can enhance the collection of anisotropic information of samples [28,29]. The polarized parametric field is obtained by the calculation of scattering field which shows a concentrated distribution at a certain spatial dimension. We can analyze the difference of optical properties among different nanoparticles by using the distributed information in parametric field such as extinction angle and phase difference [30]. In addition, the Stokes vector information can be used for mapping in the Poincaré sphere which reflects the full polarization states distribution of the sample.

3. SIMULATED RESULTS AND DISCUSSIONS

A. Simulation Model

The simulated sample model is shown in Fig. 4(a), which consists of SiO_2 substrate, gold nanoparticle and virus particle. The diameter of substrate is $0.5\mu m$ and the thickness is $0.3\mu m$.

Adenoviruses are medium-size (90-100nm), unenveloped viruses with icosahedral nucleocapsid containing a double-stranded DNA genome. Coronaviruses are a large family of viruses. Mature coronaviruses are in various forms, with a diameter of about 60-220nm. They are mainly spherical, and a few are oval or polygonal. For convenience of modelling in simulations, we here approximate the gold nanoparticle and adenovirus particle as geometric sphere in our study. The diameters of gold and virus are 100 nm and 80 nm, respectively, with their refractive index of 0.40+ i0.54 (AuNP), and 1.47 (Virus) at the wavelength of 532nm.

The light source is TFSF (Total-Field Scattered-Field) plane wave and its wavelength is 532nm. The detector uses a spherical monitor and its diameter is $0.63\mu m$, which is consistent with the object depth of objective lens. The boundary condition is set to be Perfect Matched Layer (PML) with its thickness of $0.35\mu m$. The simulation time is 1000fs, and the mesh size is chosen as 20nm.

In Fig. 4(b), we show a schematic of projection transformation from the near field to far field in DGTD. The far-field projection is used to calculate the electromagnetic field of a point in the space far from the structure that produces the light. A typical far-field projection samples the field near the radiating structure and decomposes it into spherical waves. This decomposition is then used to reconstruct the electromagnetic field at any required point in the space. The near field is usually collected in a closed surface S', sampling at a set point $\vec{r}'$, and n_b is the background refractive index shown in Fig. 4(b). Decompose the near field $\vec{E}(\vec{r}')$ and $\vec{H}(\vec{r}')$ into a set of spherical waves first, and then an equivalent set of surface currents are generated [31,32].

$$\vec{J}_s(\vec{r}') = \hat{n}(\vec{r}') \times \vec{H}(\vec{r}'). \tag{11}$$

$$\vec{M}_s(\vec{r}') = -\hat{n}(\vec{r}') \times \vec{E}(\vec{r}'). \tag{12}$$

According to the Love's equivalence principle, these equivalent surface currents contain all the information needed for a light source [31]. The far field is calculated by the equivalent surface current $\vec{J}_s(\vec{r}')$, and equivalent magnetic surface current $\vec{M}_s(\vec{r}')$. Making each point on the surface near the field as a point source and using the known analytical solution of Maxwell's equations, we can calculate the far field, which is generated by all the aggregated point sources.
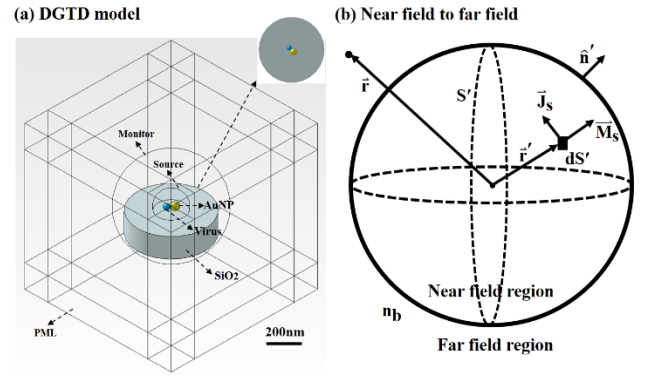

Fig. 4. (a) Sample model simulated in DGTD. (b) Diagram of transformation from near field to far field in DGTD.

B. Polarized Parameter φ

In the simulation, we injected ten linearly polarized lights with different polarization angles in turn and collected the scattering field data on spherical monitor. Considering the working distance of objective lens used in the experiment is 0.21mm, we performed the near- to far-field transformation and the distance is 0.21mm away from the nanoparticle. After such transformation, we use the PIMI calculation to obtain the polarized parameters φ, $|sin\delta|$ and Stokes vector.

Figure 5 and Figure 6 show the spherical scattering images and the curves of the polarized parameter φ simulated by DGTD in the far field. The difference of the scattering fields between a single gold particle (AuNP) and a gold-virus combination (AuNP+Virus) mainly exists in the pair of main petals on the upper hemisphere and lower hemisphere which have large scattering field and concentrated scattering intensity. Besides, we also employ four side perspectives to present the differences in the side scattering fields of different nanoparticles.

Figure 5 shows the polarization modulated scattering fields of the parameter φ on the upper and lower hemispheres. By extracting the main scattering features from the upper and lower hemispheres along the dotted circle lines, the scattering intensity curves are plotted in the polar coordinate map. It should be noted here that since the lower hemisphere's Y-axis coordinates are reversed, the polar intensity curve is also the mirror image about the azimuthal angle θ of 0° to 180° in direction. By comparing the scattering intensity curves of AuNP and AuNP+Virus, we find that the scattering intensity peaks at the azimuthal angle θ of 126° and 306° are significantly different.
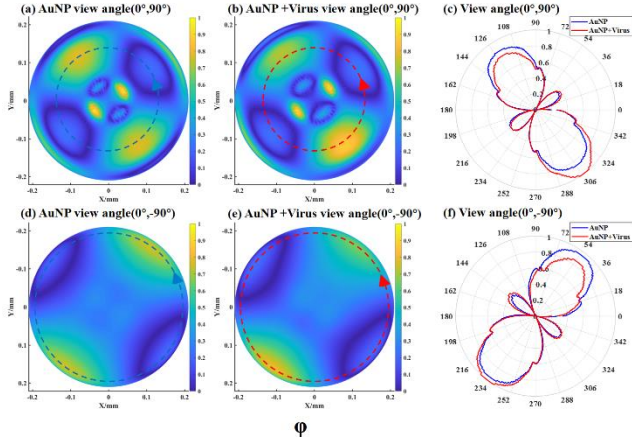
Fig. 5. Spatial scattering characteristics on the upper and lower hemispheres of the φ polarized parameter. (a, b) Feature extraction on the upper hemisphere. (d, e) Feature extraction on the lower hemisphere. (c, f) Comparison in the polar map.

Figure 6 shows the scattering fields of the parameter φ in four different side perspectives. For each view angle, we marked the extraction range of light intensity with dotted lines as virtual axis, and then compared the scattering light intensity curves of AuNP and AuNP+Virus. Via comparison, one can see that the scattering characteristics are represented in pairs of azimuth angles of 36° and 216°, 126° and 306° in the side spherical space. The scattering field of AuNP presents a symmetric distribution between pairs of angles, while that of AuNP+Virus is notably asymmetric, and the scattering information is reflected in the peak value.
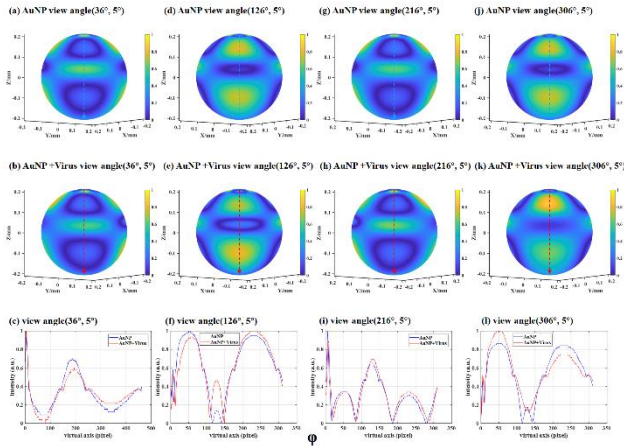

Fig. 6. Spatial scattering characteristics of the parameter φ in side space. (a-c) View angle (36°, 5°). (d-f) View angle (126°, 5°). (g-i) View angle (216°, 5°). (j-l) View angle (306°, 5°).

C. Polarized Parameter |sinδ|

Figure 7 and Figure 8 show the far-field scattering images and curves of the polarized parameter |sinδ| simulated by the DGTD. The difference of the scattering fields between a single gold particle (AuNP) and gold-virus combination (AuNP+Virus) mainly exists in the pair of main petals on the upper hemisphere and lower hemisphere, where large scattering field and concentrated scattering intensity can be seen. Besides, we also use four side perspectives to show the difference in side scattering fields of different nanoparticles. Fig. 7. shows the polarization modulated scattering fields of the parameter |sinδ| on the upper and lower hemispheres. By extracting the main scattering features from the upper and lower hemispheres along the dotted circle lines, the curves of scattering intensity are plotted in the polar coordination. Via comparing the curves of scattering intensity between AuNP and AuNP+Virus, it is clearly seen that the intensity peaks at azimuthal angle θ of 171°, 351° are significantly different.
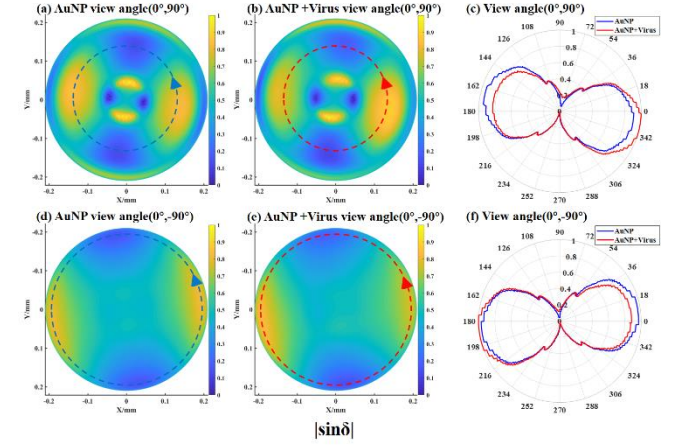

Fig. 7. Spatial scattering characteristics on the upper and lower hemispheres of the |sinδ| polarized parameter. (a, b) Feature extraction on the upper hemisphere. (d, e) Feature extraction on the lower hemisphere. (c, f) Comparison in the polar map.

Figure 8 shows the scattering fields of the parameter |sinδ| from four different side angles. For each angle of view, we mark the extraction range of light intensity with dotted lines as virtual axis, and compare the scattering light intensity curves between AuNP and AuNP+Virus. By comparing the intensity curves, it is found the scattering characteristics are represented in the two pairs of azimuth angles of spherical space. One pair is at the azimuth angle of 81° and 261°, and the other pair is at 171° and 351°. In side space, the scattering information of AuNP shows symmetric distribution, while that of AuNP+Virus is fairly asymmetric.
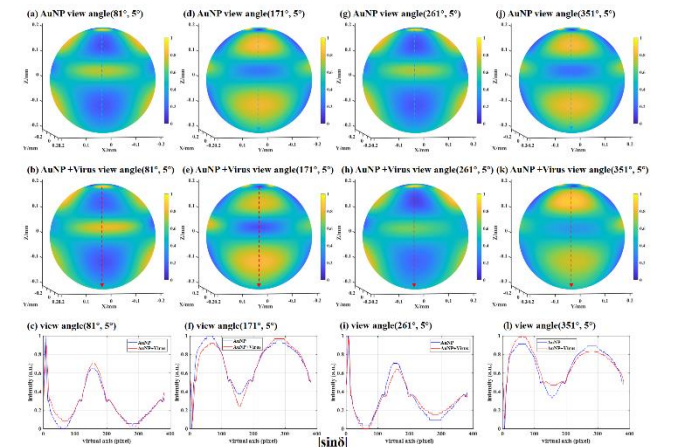

Fig. 8. Spatial scattering characteristics of parameter |sinδ| in side space. (a-c) View angle (81°, 5°). (d-f) View angle (171°, 5°). (g-i) View angle (261°, 5°). (j-l) View angle (351°, 5°).

Through the analysis of scattering fields of two polarization parameters φ and $|\sin\delta|$, which have their own specific spatial modulation directions, it is explicit that the scattering fields of AuNP+Virus are different from those of AuNP. Thus we can use the information of the peak values in these specifical spatial directions to identify the virus particles in theory. We also briefly analyzed the simulation of ellipsoidal virus particle binding to gold virus particle in DGTD and the comparison with results related to spherical virus particle is presented in Supplement 1.

4. EXPERIMENTAL RESULTS AND DISCUSSIONS

A. Polarized Fields on CCD Plane

Figure 9 shows the dependence of angles of the input polarized light on the normalized intensity values of ten images collected by the PIMI system. The theoretical calculation using Jones matrix model is compared with the experimentally measured data. From this figure, the PIMI system is consistent with the Jones theory in modulating the phase and polarization direction of scattering field.
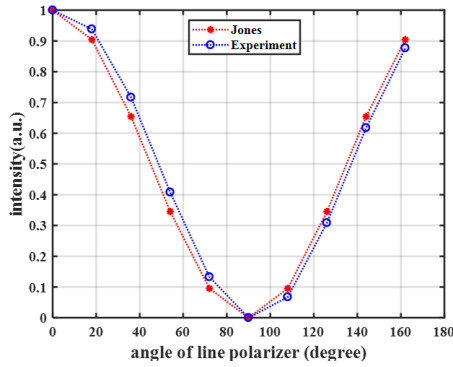

Fig. 9. The intensity curve of ten images collected from experiment compared with the Jones model calculation.

Figures 10(a) and 10(d) are two images of real AuNP and AuNP+Virus by transmission electron microscopy (TEM). Here, the substrate is SiO_2, and the diameters of the gold particle and the virus particle are 100 nm and 80 nm respectively through TEM which are taken at 200 kV on a JEM-2100.

Here, adenovirus subgroup C serotype 2 (Ad2) is used as a virus sample for detection. Adenovirus is a type of icosahedral virus that can infect the respiratory tract, gastrointestinal tract. The surface of a virus is mainly fiber, penton base, and hexon. Fiber and penton-based proteins, present at the vertices of the capsid, are involved in cell attachment and entry. Hexon, the major component of the icosahedral virus particle, comprises the facets of the virion and constitutes the bulk of the icosahedral capsid [33]. Adenovirus was purchased from Han Biotechnology co. ltd. At present, only polarization parameter imaging of adenovirus particles has been carried out in the experiment, and more types of virus samples will be used to verify our results in the future.

Figures 10(b, c) and (e, f) below illustrate the polarized parameters of nanoparticles observed using the PIMI system with an objective, where the object space numerical aperture is 0.9, the object working distance is 0.21mm and the magnification is 100×. The detector uses Basler piA2400-17 gm GigE camera, and its chip size is 2/3 inch with chip diagonal length of 11 mm. To highlight the

modulation effect of scattering field of nanoparticles, we extracted an image of 400×400 pixels on the CCD plane with each pixel size of 3.45µm, thus the size of image is about 1.38mm×1.38mm. Figs. 10(b,c) and (e,f) also show the scattering characteristics of two parametric images (φ and $|\sin\delta|$). They have a pair of petals with enhanced scattering fields. The scattering fields of φ images are concentrated along azimuthal angle from 126° to 306°, while the scattering field of $|\sin\delta|$ images are concentrated along azimuthal angle from 171° to 351°. More importantly, we can see that both the scattering fields of φ and $|\sin\delta|$ between AuNP and AuNP+Virus are visibly different in special angle direction.
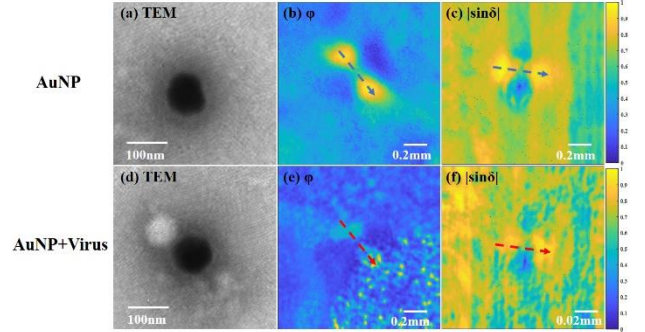

Fig. 10. The experimental data. (a, d) Transmission electron microscopy images. (b, c) Two parameter images of AuNP. (e, f) Two parameter images of AuNP+Virus.

B. Polarized Wavefront on Object Side

We know that the far-field position simulated by DGTD is on the first surface of objective lens of object side, so we invert the CCD images to the wavefront on the first surface of objective lens using ZEMAX software, and the correctness of spherical simulation can be proved by the scattering features of experimental images.

Figure 11 plots a structural model of the microscope objective, which has the same parameters as the Olympus 100× objective used in the experiment such as magnification, numerical aperture. The left side of objective lens is called the image side which is the CCD plane and the right side is the object side which is the sample position in the experimental setup. Then we make the wavefront calculation on the first surface in object side as shown in Fig. 11(b) with a dotted line by the conjugate relation. From the image side to the object side, the diameter of the exit pupil was 10.37 mm, the distance from the image plane to the exit pupil is 5.64mm.

The optical system is simulated at visible wavelength (0.48µm-0.65µm). Fig.11(c) shows the relationship between the normalized optical transfer function (OTF) values and three different line fields with 0mm, 3.9mm and 5.5mm. Fig.11(d) shows that the absolute value of distortion is less than 0.25%. Through the optical transfer function curve and distortion, we can see that the aberration of the design is within the allowable range and such design can be used in wavefront inversion.
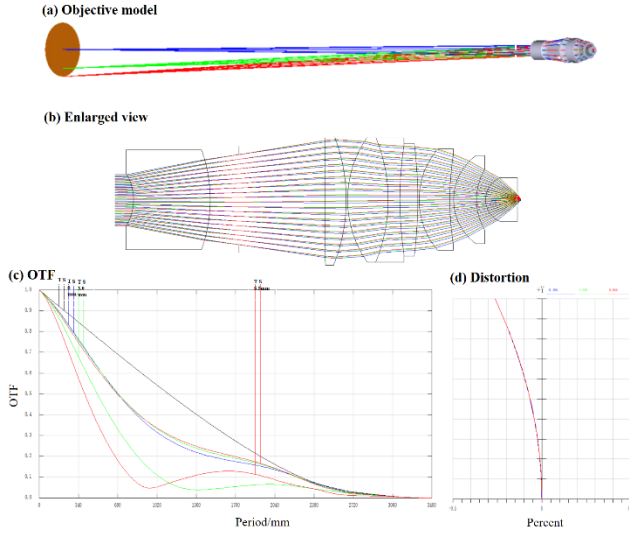
Fig. 11. Schematic of the optical lens used in the object-side wavefront calculation. (a) 100x microscopic objective lens. (b) The enlarged view to show the surface with a dotted line which calculates wavefront. (c) Optical transfer function. (d) Distortion.

The parameter wavefronts on the object-side surface are obtained through the inversion calculation according to the diameter of first surface on object-side, as shown in Figure 12. In this way, it can be well compared with the simulated spherical scattering field data which is an ideal spherical wavefront.
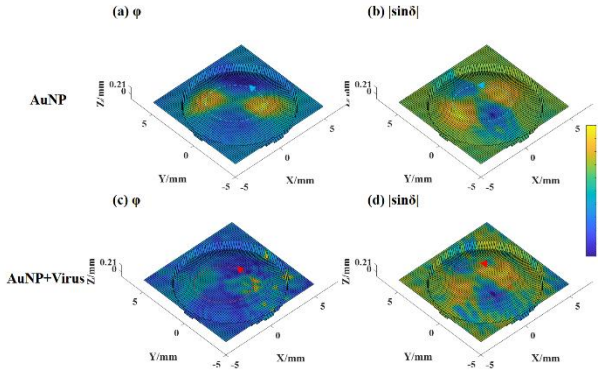

Fig. 12. The object-side surface wavefront inversed by the objective from experimental data. (a, b) The parameter wavefronts of AuNP. (c, d) The parameter wavefronts of AuNP+Virus.

Through the analysis of the scattering intensity curves of the experimental data along the circle dotted lines of curved scattering parameter field shown in Figure 13, the experimental data mainly presents as a pair of petals scattered fields which agrees well with the simulated results. We also observe that the two parametric curves of AuNP plotted with blue color is relatively symmetric, while the two parameter curves of AuNP+Virus drawn with red color are apparently asymmetrical, indicating that the adhesion of virus to the AuNP causes the prominent symmetry broken of the scattering filed and yields measurable difference in the spatial field distributions.
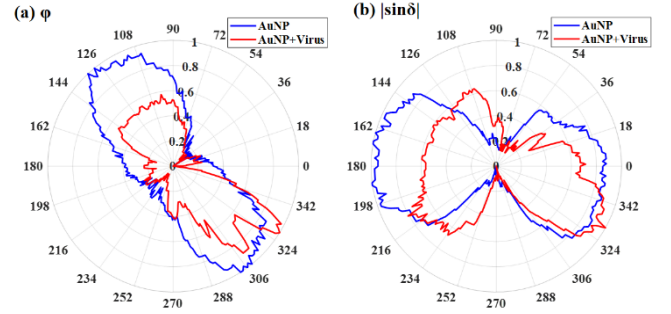

Fig. 13. The parametric curves comparison from experimental data of AuNP and AuNP+Virus. (a) φ parametric curve. (b) $|\sin\delta|$ parametric curve.

We should also point out that the transformation from near field to far field was used in DGTD simulation, so the simulated far field also has another pair of small lobes of φ and $|\sin\delta|$, which near the center on the upper and lower hemisphere due to the propagation formed in the near field. While in the experiment, the far-field microscope cannot obtain the data of the propagating near field, so there is only a pair of main far field lobes in the experiment.

Hence, the orientation of main scattering petals modulated in a certain azimuthal direction with different intensities provides a new observation basis for identifying the binding morphologies of two kinds of different particles.

C. Poincaré Sphere Representation

The Poincaré sphere can describe all the polarized states in scattering field. Each point on the sphere represents a state of polarization. Linearly polarized states lie at the equator, while elliptically polarized states fill the rest of the surface. H, V, +45, −45, LCP and RCP represent linear horizontal, vertical, +45°, -45°, left-handed and right-handed circular polarized states, respectively. The original point of the sphere is unpolarized light, and the interior of the sphere is partially polarized light except for the origin point.

In Figure 14(a), The polarization states distribution of AuNP and AuNP+Virus obtained from simulation data are mapped on a special spatial dimension in the Poincaré sphere. It is revealed that the distribution of polarization states is mainly concentrated on the upper side of the H axis, indicating that the scattering field of sample is mainly partially polarized light. The distribution of polarization states with AuNP+Virus is more diffuse than that of AuNP, showing that the introduction of virus particle indeed increases the optical anisotropy and brings new interference to the polarization scattering field.
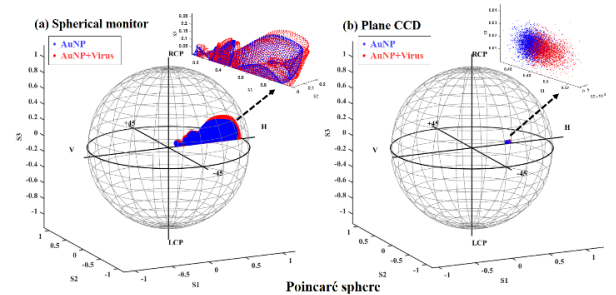

Fig. 14. Poincaré sphere mapping. (a) Polarization states from the spherical monitor in simulation data. (b) Polarization states from the experimental data on CCD plane.

Figure 14(b) depicts the distribution of polarization states corresponding to the experimental data on CCD plane. The experimental data manifests the polarization states distribution of AuNP+Virus is different from that of AuNP and they are mainly concentrated on the upper side of the H axis, which is partially polarized light. At the same time, after comparison, we also can see the spherical monitor obtains more abundant polarization states from sample scattering, which is more advantageous in detecting the scattering polarization characteristics of nanoparticles. The Stokes parameters obtained by the PIMI method were used for Poincaré sphere mapping, which could intuitively enable us to obtain the distribution positions of all the polarization states from the scattering field. The different scattering fields of the two kinds of nanoparticles are well reflected in the Poincare spheres, providing us with a basis to directly identify the existence of virus particles from the distribution of polarization states through subsequent statistical methods.

5. CONCLUSIONS

We simulated the multi-perspectives spatial polarized scattering of nanoparticles using DGTD method which could improve the collection of photons scattering information from the sample. It is found that the PIMI scattering on the upper, lower, and side spaces carry specific features of the sample structure, which is not observed in the previous detection using plane monitor.

We verify the correctness of the spherical simulation through comparison between the upper hemisphere and the wavefront inversed from the experimental data. In the experiment, the polarized parameters φ and $|\sin\delta|$ and Stokes vector of a single gold particle and gold-virus combination are compared in detail. It proves that the presence of virus particles can be identified directly from scattering distributions in the certain spatial angles.

As the results suggested, scattering photons collected from multiple perspectives can usefully help to retrieve more structural features of the sample. Owing to the merits of the relatively simple measurement system, fast detection speed, low requirements on operators and testing sites, the proposed method has marked potential in early screening of different virus particles with high speed and low cost in the hospital, communities and even public streets.

References

1. P. Rai, B. K. Kumar, V. K. Deekshit, I. Karunasagar, and I. Karunasagar, "Detection technologies and recent developments in the diagnosis of COVID-19 infection," J. Appl. Microbiol. Biotechnol. **105**, 441-455 (2021).
2. R. Samson, G. R. Navale, and M. S. Dharne, "Biosensors: frontiers in rapid detection of COVID‑19," 3 Biotech **10**, 1-9 (2020).
3. D. Pradhana, P. Biswasroya, P. K. Naik. G. Ghosha, and G. Rath, "A review of current interventions for COVID-19 prevention," Arch. Med. Res. **5**, 363-374 (2020).
4. J. F. W. Chan, C. C. Y. Yip, and K. K. W. To. "Improved molecular diagnosis of COVID-19 by the novel, highly sensitive and specific COVID-19-RdRp/Hel real-time reverse transcription-PCR assay validated in vitro and with clinical specimens," J. Clin. Microbiol. **5**, 1-33 (2020).
5. Y. Wang, H. Kang, X. Liu, and Z. Tong, "Combination of RT-qPCR testing and clinical features for diagnosis of COVID-19 facilitates management of SARS-CoV-2 outbreak," J. Med. Virol. **92**, 538-539 (2020).
6. S. Souf. "Recent advances in diagnostic testing for viral infections," Biosci. Horiz. **9**, 1-11 (2016).
7. N. C. Güler, I. Tosun, and F. Aydin, "The identification of meyerozyma guilliermondii from blood cultures and surveillance samples in a university hospital in northeast turkey: a ten-year survey," J. Mycol. Med. **27**, 506-513 (2017).
8. K. Lewandowski, Y. Xu, S. T. Pullan, S. F. Lumley, and D. Foster. "Metagenomic nanopore sequencing of influenza virus direct from clinical respiratory samples," J. Clin. Microbiol. **58**, 1-15 (2020).
9. Q. He, Z. Zhu, L. Jin, L. Peng, W. Guo, and S. H, "Detection of HIV-1 p24 antigen using streptavidin-biotin and gold nanoparticles based immunoassay by inductively coupled plasma mass spectrometry," J. Anal. At. Spectrom. **29**, 1477-1482 (2014).
10. Y. Shen, T. B. Anwar, and A. Mulchandani. "Current status, advances, challenges and perspectives on biosensors for COVID-19 diagnosis in resource-limited settings," Sens. Actuator Rep. 100025, (2021).
11. H. Zhu, Z. Fohlerová, J. Pekárek, E. Basova, and P. Neužil, "Recent advances in lab-on-a-chip technologies for viral diagnosis," Biosens. Bioelectron. **153**, 1-28 (2020).
12. J. Lukose, S. Chidangil, and S. D. George. "Optical technologies for the detection of viruses like COVID-19: progress and prospects," Biosens. Bioelectron. **178**, 1-10 (2021).
13. H. Zhang, X. Jin, H. Zhao, Y. Lin, X. Li, and L. Hou, "Photo scattering signal amplification in gold-viral particle ligation towards fast infection screening," IEEE Photonics J. **13**, 1-9 (2021).
14. M. Srivastava, N. Srivastava, P.K. Mishra, and B. D. Malhotra, "Prospects of nanomaterials-enabled biosensors for COVID-19 detection," Sci. Total Environ. **754**, 142363 (2021).
15. R. Medhi, P. Srinoi, N. Ngo, H. V. Tran, and T. R. Lee, "Nanoparticle-based strategies to combat COVID-19," ACS Appl. Nano Mater. **3**, 8557-8580 (2020).
16. M. S. Draz, and H. Shafiee. "Applications of gold nanoparticles in virus detection," Theranostics **8**, 1985-2017 (2018).
17. D. M. Sullivan. Electromagnetic Simulation Using the FDTD Method, 2nd ed. (Wiley, 2013).
18. L. Cheng, G. Zhu, G. Liu, and L. Zhu, "FDTD simulation of the optical properties for gold nanoparticles," Mater. Res. Express **7**, 1-9 (2020)
19. S. Descombes, C. Durochat, S. Lanteri, L. Moya, C. Scheid, and J. Viquerat, "Recent advances on a DGTD method for time-domain electromagnetics," Photonic Nanostruct **4**, 291-302. (2013)

20. J. Hesthaven, and T. Warburton. "Nodal high-order methods on unstructured grids. I. time-domain solution of Maxwell's equations," J. Comput. Phys. **181**, 186–22 (2002).

21. J.S. Hesthaven, T. Warburton. Nodal Discontinuous Galerkin Methods: Algorithms, Analysis, and Applications, (Springer, 2008).

22. J. Chen, and Q. H. Liu. "Discontinuous Galerkin time-domain methods for multiscale electromagnetic simulations: a review," Proc. IEEE **2**, 242-254 (2013).

23. M. König, K. Busch, and J. Niegemann. "The discontinuous Galerkin time-domain method for Maxwell's equations with anisotropic materials," Photonics and Nanostructures-Fundamentals and Applications **8**, 303-309 (2010).

24. D. Shree, B. Malakareddy, K. Uralakatte, B. Rajan, and N. Krishnaswamy, "DGTD modelling of Mie scattering phenomenon of gold nano particles of biosensing applications," Proc. SPIE, Clinical Biophotonics, **11362**, 1-8 (2020).

25. L. D. Angulo, J. Alvarez, M. F. Pantoja, S. G. Garcia, and A. R. Bretones, "Discontinuous Galerkin time domain methods in computational electrodynamics: state of the art," in Forum for Electromagnetic Research Methods and Application Technologies, (2015). p. 1-23.

26. M. A. Geday, W. Kaminsky, J. G. Lewis, and A. M. Glazer. "Images of absolute retardance L·Δn, using the rotating polariser method," J. Microsc. **198**, 1-9 (2000).

27. R. Ossikovski, J. J. Gil, and I. San José. "Poincaré sphere mapping by Mueller matrices," J. Opt. Soc. Am. A. **30**, 2291-2304 (2013).

28. X. Liu, B. Qiu, Q. Chen, Z. Ni, Y. Jiang, M. Long, and L. Gui, "Characterization of graphene layers using super resolution polarization parameter indirect microscopic imaging," Opt. Express **22**, 20446-20456 (2014).

29. W. Liu, J. Xiong, H. Zhang. X. Liu, G. Liu, and H. Zhao, "Characterization of Komagataeibacter xylinus by a polarization modulation imaging method," J. Phys. D Appl. Phys. **53**, 1-9 (2020).

30. K. Ullah, X. Liu, M. Habib, and Z. Shen, "Subwavelength far field imaging of nanoparticles with parametric indirect microscopic imaging," ACS Photonics **5**, 1388-1397 (2018).

31. D. Sullivan, and J. L. Young. "Far-field time-domain calculation from aperture radiators using the FDTD method," IEEE Trans. Antennas Propag. **49**, 464-469 (2001).

32. X. Li, A. Taflove, and V. Backman. "Modified FDTD near-to-far-field transformation for improved backscattering calculation of strongly forward-scattering objects," IEEE Antenn. Wirel. Pr. **4**, 35-38 (2005).

33. J. J. Rux, R. M. Burnett. "Adenovirus structure," Human Gene Therapy, **15**, 1167 (2004).